Toward Standard Radiosonde Observations of Waves and the Mean State in the 30–40-km Altitude Range Using 3-kg Balloons

TAKENARI KINOSHITA,[a] SHIN-YA OGINO,[a] JUNKO SUZUKI,[a] RYUICHI SHIROOKA,[a] TAKUJI SUGIDACHI,[b] KENSAKU SHIMIZU,[b] AND MATTHEW H. HITCHMAN[c]

[a] *Japan Agency for Marine-Earth Science and Technology, Kanagawa, Japan*
[b] *Meisei Electric Co. Ltd., Gunma, Japan*
[c] *University of Wisconsin–Madison, Madison, Wisconsin*

(Manuscript received 5 February 2021, in final form 9 March 2022)

ABSTRACT: Observations of temperature and wind velocity in the 30–40-km altitude layer have been sparse since elimination of the standard rocketsonde sounding network in the 1990s. In an effort to extend the vertical range of radiosonde observations into the upper stratosphere, experiments were conducted with a 3-kg balloon at Tsukuba, Japan, on 5 November 2019. Using this relatively inexpensive balloon technology, four radiosondes were launched, with two reaching above 40-km altitude. These profiles were compared with satellite and reanalysis data in the 30–40-km layer, which showed an overall good agreement and an ability of radiosondes to capture shorter vertical-scale variations. The ability to quantify gravity wave parameters from the data is described, with application to wave events detected near 38–40 km. This type of balloon will be deployed extensively in an upcoming intensive observation campaign over the Maritime Continent, which will contribute toward achieving standard radiosonde observations in the 30–40-km altitude range. This system extends the ability to provide information regarding gravity wave and planetary wave activity upward to ~40 km.

KEYWORDS: Gravity waves; Radiosonde/rawinsonde observations; Oscillations

1. Introduction

Long-range global forecasting, global climate models, and diagnosis of the general circulation of the middle atmosphere all require accurate measurements of atmospheric waves of various scales, including gravity waves excited by convection, topography, and geostrophic adjustment, which are found throughout the middle atmosphere. These waves drive the atmospheric general circulation through their dissipation and breaking and play an important role in transporting atmospheric minor components from the tropics to the poles (e.g., Butchart 2014). Together with planetary-scale waves, gravity waves help to determine the Brewer–Dobson circulation and phenomena such as sudden stratospheric warmings (SSWs), which can affect tropospheric weather (e.g., Kodera et al. 2011; Baldwin et al. 2021). In the tropics, they help to create the semiannual oscillation (SAO) and quasi-biennial oscillation (QBO) (e.g., Hirota 1980; Baldwin et al. 2001). Sudden stratospheric warmings and the QBO, in turn, have been shown to affect tropical convective activity (Nishimoto and Yoden 2017). Thus, understanding wave activity in the middle and upper stratosphere will lead to a more detailed understanding of not only the material transport in that region, but also climate change and weather phenomena in the troposphere.

In the upper stratosphere, there is a relative lack of in situ measurements. Daily observational depictions of the middle and upper stratosphere include satellite observations of temperature and chemical substances including ozone, lidar observations of temperature, and radar observations of wind velocity. Essential observations of wind velocity, temperature, and pressure from the ground to the middle stratosphere are currently routinely obtained by radiosondes, but they generally reach only to ~30-km altitude. Recently, Dörnbrack et al. (2018) achieved a height of 38.1 km with a 3-kg balloon on 30 January 2014 during the GW-LCYLCE 2 campaign and a height of 39.4 km with a 3-kg balloon on 30 September 2019 during the SouthTRAC campaign. The present work is a contribution toward extending the vertical range of the global radiosonde network coverage upward to include the 30–40-km layer, with application to observations of wave structure.

Satellite observational capabilities have steadily increased since the meteorological satellite *TIROS-1* was launched in 1960 (Stroud 1960). The *UARS* satellite, launched in October 1991 from the space shuttle, has provided measurements of chemical substances, stratospheric wind, and temperature until it was decommissioned in December 2005 (Reber et al. 1993). Currently, there are *Odin*, *Aura*, and *TIMED* for observation of the middle to upper stratosphere, and they observe temperature and chemical substances (Murtagh et al. 2002; Froidevaux et al. 2006; Mlynczak et al. 2007). Regarding instruments capable of observing wind velocity in the middle and upper stratosphere, the Stratospheric Inferred Winds (SIW) instrument is scheduled to be launched by Sweden in 2022 (Baron et al. 2018).

In operational radiosonde observations, a rubber balloon bursts when it reaches the height of about 30 km, so data are

Denotes content that is immediately available upon publication as open access.

Corresponding author: Takenari Kinoshita, t-kinoshita@jamstec.go.jp

DOI: 10.1175/JTECH-D-21-0011.1

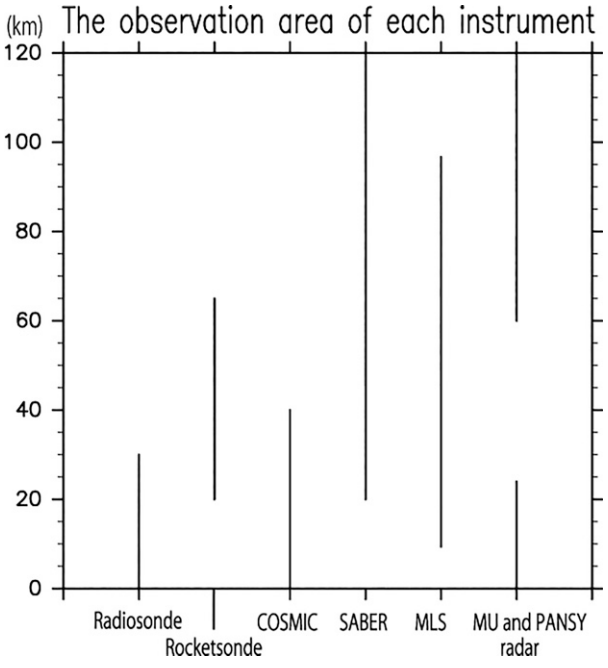

FIG. 1. Vertical range of observations for traditional radiosonde, rocketsonde, selected satellite instruments (COSMIC, SABER, and MLS), and larger atmospheric radar (MU and PANSY radars) from the ground to 120 km.

obtained from the ground to the height of 30 km. At higher altitudes, rocketsonde observations (20–65 km) were carried out from the 1960s to the 1990s (e.g., Baldwin and Gray 2005), and then intermittently in India and China (Zhou et al. 2017; Das et al. 2016). The vertical resolution of rocketsonde observation is about 2 km, and it is difficult to capture gravity waves having short vertical wavelength.

On the other hand, superpressure balloons and zero-pressure balloons made of plastic film (e.g., polyethylene film) that can be observed for a long time in the stratosphere are being used in various countries around the world (e.g., the Strateole, Vorcore, and Concordiasi campaigns). Experiments have been conducted in the Antarctic and equatorial regions, which investigated the polar vortex, the QBO (alternating layers of descending eastward and westward zonal winds), convective activity, and atmospheric waves. In a high-altitude observation experiment using a plastic film balloon, the Japan Aerospace Exploration Agency (JAXA) recorded a maximum altitude of 53.7 km on 20 September 2013 (Fuke 2017). Since these plastic film balloons are more expensive than rubber balloons, it is hard to launch them as frequently as the operational radiosonde observations. In addition, although lidars (e.g., Park et al. 2006) and large atmospheric radars such as the MU and PANSY radars (e.g., Fukao et al. 1985; Sato et al. 1997, 2014) are powerful tools to observe temperature and wind velocity, respectively, with high resolution, their high cost makes them unsuitable for multipoint observations.

The vertical range of observations for traditional radiosonde, rocketsonde, radar, and satellite instruments used for comparison in this study are shown in Fig. 1. These include data from the Constellation Observing System for Meteorology, Ionosphere and Climate (COSMIC)-2 mission (UCAR COSMIC Program 2019), the Sounding of the Atmosphere using Broadband Emission Radiometry (SABER; Russell et al. 1999), and the Earth Observing System Microwave Limb Sounder (MLS; Schwartz et al. 2015), as well as large atmospheric radars (MU and PANSY). From considering the range of observational capabilities at present, one may see that it remains a challenge to obtain good information, including both wind velocity and temperature above 30-km altitude.

Because of this situation, progress in understanding phenomena in the middle and upper stratosphere has been delayed. Although reanalysis data have recently been improved in spatiotemporal resolution, the vertical resolution of the input satellite information is generally too coarse to analyze wave activity. Above this region, there is a lack of observational data. The SAO in equatorial zonal wind exists in the upper stratosphere to upper mesosphere, with a period of 6 months, and is characterized by descending layers of eastward winds alternating with westward winds arising from cross-equatorial advection at the solstices, centered near the stratopause (Hitchman and Leovy 1986). Recently, Kawatani et al. (2020) compared the representations of the SAO within six reanalysis datasets and with the SABER and MLS observations. They found large differences among reanalyses in the SAO region and showed that the zonal wind standard deviation is smallest around the longitude of Singapore, where consistently high-quality radiosonde observations are available.

Thus, obtaining wind velocity and temperature data in the stratosphere, especially with high vertical resolution, on an ongoing basis, and at multiple points, is necessary for investigating wave activity, the SAO, and their interaction. By assimilating data with high vertical resolution at altitudes from 30 to 40 km at multiple points into atmospheric general circulation model and forecast models, we think the accuracy of the stratospheric circulation will be improved and more correctly represent the detailed behavior during extreme events such as sudden stratospheric warming. In addition, including such data may contribute to improving the accuracy of long-term forecasts by continuous assimilation of long-term observations.

To establish the method of high-altitude radiosonde observations, 3- and 4-kg balloons, which are 6–15 times as large as operational balloons, were experimentally attached to radiosondes at the Tsukuba release field to directly observe wind velocity and temperature to an altitude of 40 km or more above the ground. Observations using the 3- and 4-kg balloons have the following merits.

1) The vertical structure of atmospheric waves can be captured from the ground to high altitude continuously.
2) By observing wind velocity and temperature up to the height of 40 km, not only the QBO but also the lower portion of the SAO can be directly sampled.
3) Atmospheric waves with small vertical scales can be investigated using wind velocity and temperature data with high vertical resolution.

4) Not only is the cost comparatively moderate (about twice as much as the traditional release cost), but the observation method used in the field is easy to prepare because the operational radiosonde receiving, and release system can be used. Frequent observations are possible at multiple points.

In this observation, four test launches were conducted. Two of the four ascents achieved a height of more than 40 km. These exceeded the heights of 38.1 and 39.4 km recorded by Dörnbrack et al. (2018) and provide complementary, new observations regarding ascents with a 3-kg balloons. (For comparison, their data are available at https://www.pa.op.dlr.de/southtrac/news/2019/09/30/last-balloon-soundings-and-one-more-upcoming-local-flight/.)

In this study, we report the observational results obtained from four test launches and the results of analysis of the wave activity observed in the altitude range of 38–40 km.

2. Detail of experimental observation

The experimental observations were conducted at the Tsukuba release field in Moriya City, Ibaraki, Japan (35.93°N, 140.00°E), with the cooperation of Meisei Electric Co. Ltd., in preparation for the enhanced observation campaign of Years of the Maritime Continent–Boreal Summer Monsoon (YMC-BSM) scheduled for 2021. The YMC campaign is a multiyear (2017–21) international program to expedite the progress toward improving understanding and prediction of the local oceanic and atmospheric multiscale variability in the Indo-Pacific Maritime Continent weather–climate system and its global impacts (Yoneyama and Zhang 2020). The release times were at 1700 Japan standard time (JST) (0800 UTC), 2000 JST (1100 UTC), and 2300 JST (1400 UTC) 5 November 2019 and 0200 JST 6 November (1700 UTC 5 November). Note that the four test launces were conducted at night to avoid the effects of solar radiation. The weather was fine and the wind on the ground was almost 0 m s^{-1}. The radiosondes used in this observation were iMS-100 (~40 g). A TOTEX 3000-g balloon (TX3000) was used for the first three launches, where the buoyancy, i.e., the lifting force beyond that which balances the weight of balloon and gas, was set to 1600, 1000, and 2000 g, respectively. In the fourth launch, a TOTEX 4000 g balloon (TA4000) was used and the buoyancy was 2000 g. The flight configuration consisted of a parachute located 7.5 m from the balloon, with a 30-m unwinder connecting to the iMS-100. In this experiment, helium gas was used. The ascent velocity was different for each release, due to differences in buoyancy, but it was in the range 3–7 m s^{-1} for the first and second releases and 5–8 m s^{-1} for the third and fourth releases. Note that we think the effect of balloon with a 30-m unwinder on temperature error is adequately small (less than 0.2 K) at night, although the effect in day can be large (e.g., Tiefenau and Gebbeken 1989). Since the radiosonde took observations every second, the vertical resolution the of raw data is about 5–6 m. The horizontal velocity and temperature resolutions of the iMS-100 sondes are 0.01 m s^{-1} and 0.1 K, respectively. Note that the temperature resolution gets worse with increasing altitude in the stratosphere, requiring comparison with other data. This is due to the time constant of the temperature sensor and is described in the next section. Note also that the light payload in the experiment has the possibility to consistently reach heights above 40 km. To achieve higher-altitude radiosonde flights, one possibility is to reduce the total weight of objects launched in a sounding. Since the radiosonde and unwinder are already light enough, it may be necessary to reduce the balloon weight, keeping its strength.

Wind and temperature profiles were obtained from the following global modeling and satellite datasets: ERA5 data, available from https://cds.climate.copernicus.eu/cdsapp#!/dataset/reanalysis-era5-pressure-levels?tab=overview, and MERRA-2 assimilated meteorological fields V5.12.4, available at https://goldsmr5.gesdisc.eosdis.nasa.gov/data/MERRA2/M2I3NPASM.5.12.4/2019/11/, JRA-55 data from https://jra.kishou.go.jp/JRA-55/index_en.html#usage. Temperature profiles were also obtained from COSMIC data, from https://data.cosmic.ucar.edu/gnssro/cosmic2/nrt/level2/2019/310/atmPrf_nrt_2019_310.tar.gz, SABER data, from ftp://saber.gatsinc.com/custom/Temp_O3_H2O/v2.0/SABER_Temp_O3_H2O_November2019_v2.0.nc, and MLS data from https://acdisc.gesdisc.eosdis.nasa.gov/data/Aura_MLS_Level2/ML2T.004/2019/MLS-Aura_L2GP-Temperature_v04-23-c01_2019d310.he5.

The high-altitude radiosonde observation data are available from the YMC data repository at http://www.jamstec.go.jp/ymc/. The GFD-DENNOU library was used for drawing figures.

3. Results

a. *Overview of observational data*

Figure 2 shows vertical profiles of zonal and meridional wind velocities, and temperature obtained from four experimental observations. Considering instrument response times and the pendulum-related and small fluctuations that will be seen in the analysis of the next subsection, we applied a 20-s low-pass filter to the raw data. The first launch exceeded the geometric height of 40 274 m, and the third reached the height of 40 655 m. The second and fourth reached 37 852 and 33 342 m, respectively. From these results, it is a high probability that a radiosonde with a buoyancy of 1600–2000 g would routinely exceed an altitude of 40 km for a 3-kg balloon, although this has not been proven statistically and will be evaluated by the YMC campaign.

From the zonal wind velocities shown in Fig. 2, the jet stream is located at the height of about 12 km, with a speed of about 50 m s^{-1}. It can be seen that the vertical temperature gradient becomes less than -2 K km^{-1} around the height of 10 km, corresponding to the tropopause. Note that the WMO thermal tropopause definition is "the lowest level at which the lapse rate decreases to 2°C km^{-1} or less, provided also the average lapse rate between this level and all higher levels within 2 km does not exceed 2°C km^{-1}" (WMO 1957) and the center of jet stream is above the tropopause in this observation. This is typical for locations near and poleward of the subtropical jet core. The temperature continues to decrease in the height range 11–17 km, with minima in the 18–20-km layer, which is a feature of the winter stratosphere.

We now consider wave signals with vertical wavelengths of 2–4 km. These signals are considered to include gravity waves

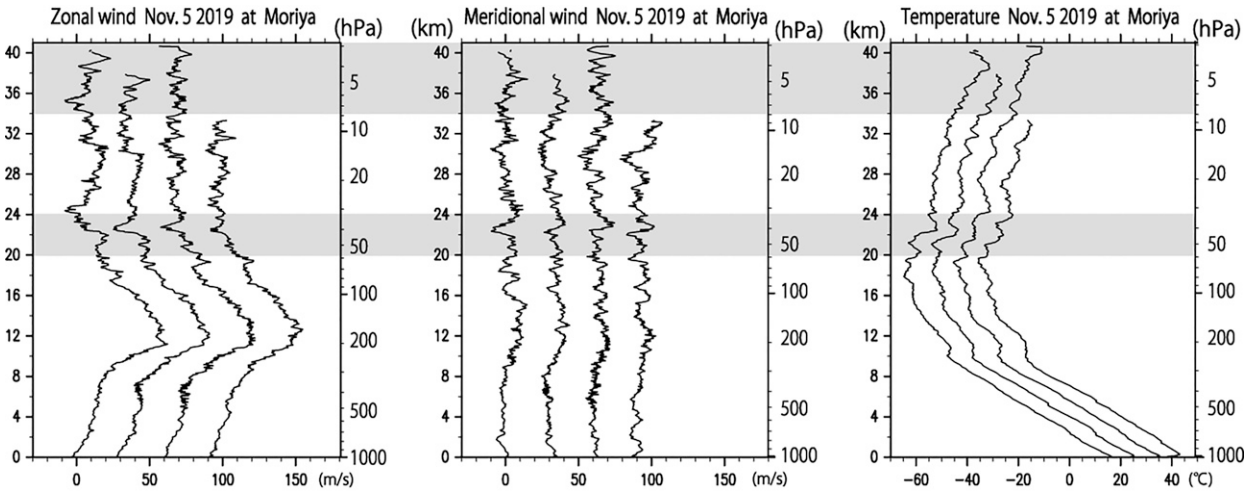

FIG. 2. Time series of vertical profiles of observed (left) zonal wind, (center) meridional wind, and (right) temperature. Each subsequent profile is displaced by +30 m s^{-1} for zonal and meridional wind and by +10°C for temperature. Shaded regions highlight the layer where large disturbances can be seen.

and are seen in the layers 20–24, 34–37, and 38–40 km (shaded regions of Fig. 2), which appear in both the wind velocity and temperature data. In addition, a large disturbance with a vertical wavelength of about 10 km can be seen in the first and second zonal wind velocity profiles. In these profiles, zonal wind speed decreases above the subtropical westerly jet near 12 km to near 0 m s^{-1} at ~24 km, with a very slight increase in westerly flow in the 24–40-km layer, well equatorward of the core of the developing polar night jet.

Figure 3 shows vertical profiles of observed ascent rate. The average ascent rate is found to be 5–6 m s^{-1}. The ascent rate decreased as the altitude approached 40 km, and in the second launch it was almost 0 m s^{-1} at the height of 37 852 m and could not gain any more altitude. Note that the balloon stayed intact for a while after reaching maximum altitude in the second launch, but that these data were not used in this study. Note also that the ascent rate includes measurement errors of radiosonde altitude or changing drag coefficient of the balloon for small fluctuations (Gallice et al. 2011; Zink and Vincent 2001) and the ascent rate fluctuations are associated with relatively high-frequency gravity waves, while horizontal wind fluctuations are a response to low-frequency gravity waves. Since we focus on the relatively low-frequency gravity waves in this study, the ascent rate was not used in the analysis of gravity waves.

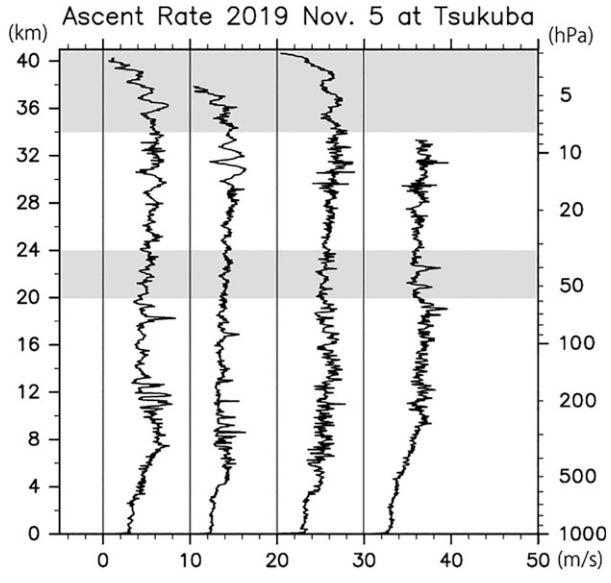

FIG. 3. Time series of vertical profiles of observed ascent rate. Each subsequent profile is displaced to the right by +10 m s^{-1}. Shaded regions highlight the layers where large disturbances can be seen.

As a balloon ascends through a varying vertical motion field, buoyancy oscillations may be excited. Variations of ~2–4 m s^{-1} in vertical velocity, with vertical wavelength ~2 km are seen at many levels in Fig. 3. Although these variations in the ascent rate include measurement errors, the variations may be attributable to buoyancy oscillations due to gravity waves and are superimposed on a mean ascent rate.

The ascent rate decreases significantly approaching maximum altitude, suggesting that the force associated with the expansion of the balloon during ascent is almost balanced by the tension of the rubber of the balloon. As the ascent rate becomes smaller, the drift distance due to horizontal winds to reach a certain altitude becomes larger. However, more observations of high-altitude radiosondes are necessary to determine the characteristics of this phenomenon.

b. Comparison with satellite and reanalysis data from 30 to 40 km

Regarding accuracy of the obtained wind velocity data, the positioning information from GPS satellites is stable at high altitudes (but not for the lowermost altitudes), and the vertical resolution of wind velocity data is also stable at high altitudes. However, it is necessary to pay attention to the accuracy and resolution of temperature data at high altitude

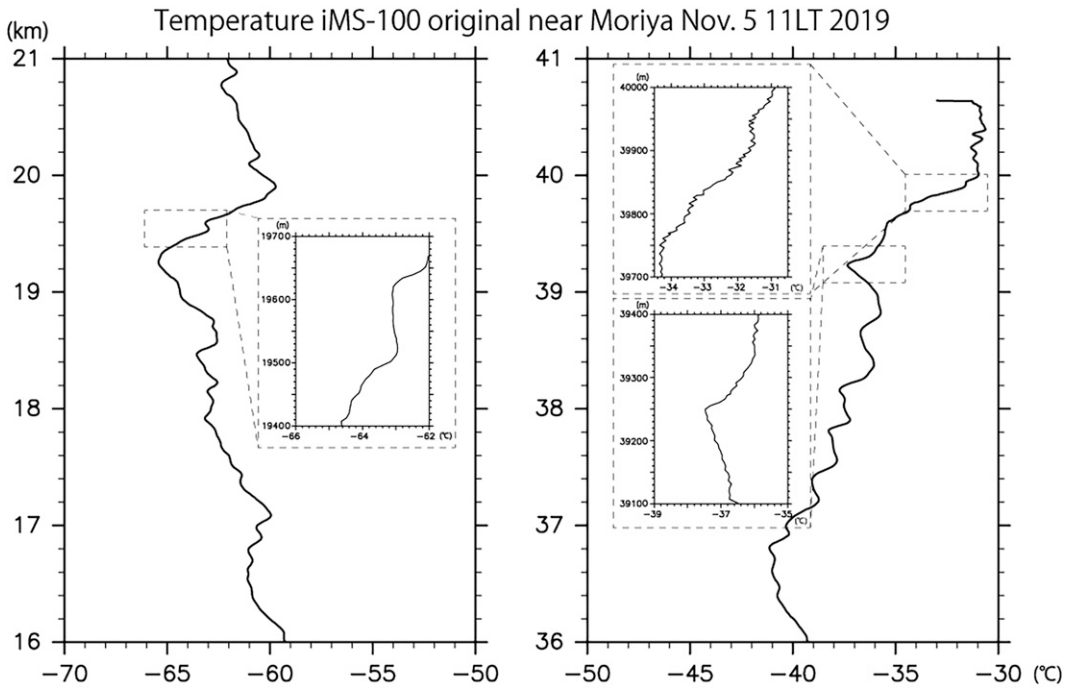

FIG. 4. Vertical profiles of temperature (left) from 16 to 21 km and (right) from 36 to 41 km. Enlargements of the three altitudes are also shown.

since the longer time constant of the sensor contributes to uncertainties, as the atmospheric density decreases. Note that the time constant of the sensor is about 0.4 s on the ground, and about 2.4 s at 10 hPa. To confirm the temperature behavior, the unfiltered temperature data in the altitude range 16–21 km and 36–41 km at 2300 JST (1400 UTC) 5 November, when the radiosonde reached its highest altitude, are plotted in Fig. 4. Enlargements of temperature profile details for the layers 19 400–19 700, 39 100–39 400, and 39 700–40 000 m are also shown. It is found that the temperature profile near 40 km contains fine structures compared to the other profiles. To consider the factors contributing to the difference, the ascent rates in the same altitude ranges are shown in Fig. 5. The ascent rates for 19 400–19 700 and 39 100–39 400 m are almost 5–6 m s^{-1}. On the other hand, the ascent rate for 39 700–40 000 m is almost 4 m s^{-1} and has smaller oscillation than the other profiles. From a comparison between temperature and ascent rate profiles, it is suggested that the small ascent rates and the small oscillations contribute to the part of the fine structure of the temperature near 40 km. The small oscillations may be due to the pendulum motion between the balloon and the instrument. Moreover, the fine structure may also include the effect of 0.1 K measurement resolution of the sensor. Therefore, although the fine structure found in the temperature data is possible to contain small disturbances that actually exist, they are affected by the above-mentioned factors and the low-pass filter will be applied in the rest of analysis to eliminate the effect. At an altitude above 40.4 km, the ascent rate decreases to zero without oscillation. On the other hand, the temperature data show a sharp decrease near the highest altitude. This may indicate that the ascent rate is close to zero and the temperature is not being measured properly, which requires attention.

For comparison with multiple reanalysis and satellite data, it is important to consider the vertical resolution of reanalysis and satellite data (Table 1). We used data which were low-pass filtered with a window of 400 s instead of 20 s. Figure 6 shows the trajectories of radiosonde observations and observation points of satellites used in this study. Each of the four radiosondes drifted eastward and were located between 141.2° and 142.2°E in the altitude range 30–40 km. The SABER observation was the closest to the radiosonde observations, of all satellite observations used in the comparison, but all satellites were located within 200 km.

Figure 7 shows vertical profiles of zonal and meridional wind velocities, and temperature from ERA5, the latest atmospheric reanalysis data produced by the European Centre for Medium-Range Weather Forecasts (Hersbach et al. 2018) (green), Modern-Era Retrospective Analysis for Research and Applications, version 2 (MERRA-2; GMAO 2015) (blue), the Japanese 55-year Reanalysis (JRA-55; Kobayashi et al. 2015) (red), and radiosonde (black). Note that the ERA5 in this study uses data from the model levels, which are converted to geometrical heights and plotted. The ERA5 and radiosonde observation data are plotted at 2300 JST (1400 UTC) 5 November. The MERRA-2 and JRA-55 data are plotted at 0000 JST (1500 UTC) and 0300 JST 6 November (1800 UTC 5 November), respectively. These reanalysis profiles are plotted with corrections using the four points closest to the radiosonde's position at the height from 30 to 40 km.

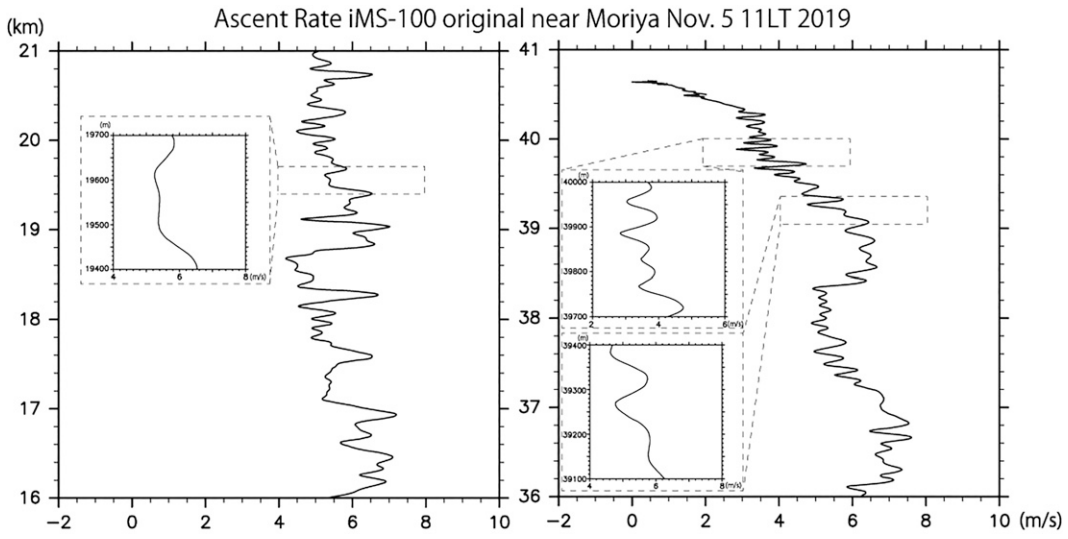

FIG. 5. As in Fig. 4, but for ascent rate.

Note that the conversion to pressure coordinates of radiosonde observations was calculated by converting the geometrical height to the geopotential height and using the hydrostatic approximation. Note also that the respective pressures corresponding to highest altitudes reached by the new radiosonde observations are 2.60, 3.66, 2.45, and 7.01 hPa. As an overview, it is found that these reanalysis data are almost consistent with radiosonde observations for temperature, although ERA5 and MERRA-2 temperatures are warmer than JRA-55 temperature above 5 hPa. For zonal and meridional wind velocity, the difference between radiosonde observation and reanalysis data is small and meridional wind velocity of ERA5 data captures the basic-state vertical structure seen in the radiosonde observation.

Figure 8 shows vertical profiles of the differences of zonal wind, meridional wind, and temperature between the radiosonde observations and reanalysis data shown in Fig. 7. For the wind velocity data, the difference is less than 5 m s^{-1}. Among the reanalysis datasets, ERA5 is the closest to the observed data in the meridional wind velocity. The difference of temperature is less than 3 K for most heights. It is found that JRA-55 is closest to the observed data. These differences are thought to be due to disturbances having large amplitude in the stratosphere. Another contribution to differences likely comes from aliasing of the significant gravity wave signal through coarser vertical sampling in the reanalyses.

Figure 9 shows that vertical profiles of temperature and temperature difference between satellite data and radiosonde data at 2300 JST 5 November 2019. The satellite data used in this study are from the COSMIC-2 mission, with the selected profile located at 137.43°E, 36.88°N at 0440 JST 6 November, and a profile from the SABER instrument on the *TIMED* satellite located at 35.70°N, 142.37°E at 0705 JST 6 November, and one from the MLS on the *Aura* satellite located at 35.57°N, 140.38°E at 0213 JST 6 November (Fig. 6). In the layer 30–40 km, the temperature of MLS is closest to that of the observation data and its difference is about ±2 K. On the other hand, the temperature of COSMIC is about 3 K higher and SABER is about 5 K lower than the radiosonde observation data at pressures above 5 hPa. From these results, the new radiosonde observations, including for temperature, were found to be close in value to the reanalysis data and satellite

TABLE 1. Horizontal resolution and pressure-level points of reanalysis data and vertical resolution of the satellite data for 30–40 km.

Data	Horizontal resolution	Pressure-level points or vertical resolution
ERA5	0.25°	10, 7, 5, 3, and 2 hPa
MERRA-2	0.5° lat, 0.625° lon	10, 7, 5, 4, 3, and 2 hPa
JRA-55	1.25°	10, 7, 5, 3, and 2 hPa
COSMIC	~300 km	~0.5 km
SABER	~400 km	~2 km
MLS	165 km	4 km

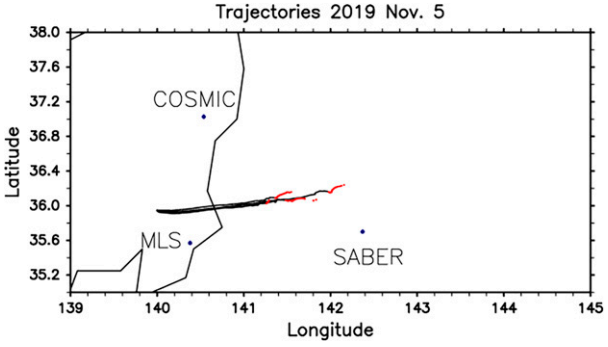

FIG. 6. Horizontal map of the trajectories of radiosonde observations and satellite observation points for COSMIC, SABER, and MLS. The black lines represent the trajectories from the ground to the height of 30 km, and the red lines represent the trajectories above the height of 30 km.

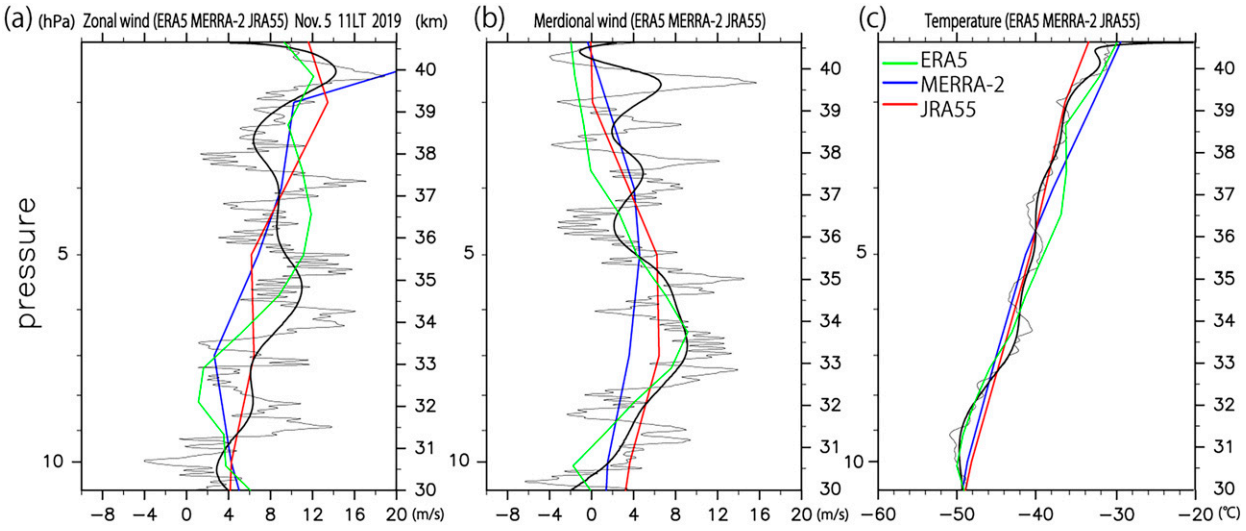

FIG. 7. Vertical profiles of (a) zonal wind, (b) meridional wind, and (c) temperature of ERA5 (green), MERRA-2 (blue), JRA-55 (red), and radiosonde observation data with a 400-s low-pass filter (thick black line) and 20-s low-pass filter as in Fig. 2 (thin black line).

data, even below 10 hPa. The radiosonde instrument uncertainty is 0.4 K for temperature at night and 1–3 m s^{-1} for wind speed (Kizu et al. 2018), which is adequately smaller than the difference between radiosonde observation data and the reanalysis and satellite data. Including this, we think that the radiosonde observation data in the range 30–40 km are at least sufficient for the analysis of atmospheric waves in the next section, although a number of observations are needed to confirm if the data can contribute to accurate observations and global analyses in the range of 30–40 km.

c. *Analysis of disturbance around 40 km*

There are a number of studies on wave activity using radiosonde data with high vertical resolution, such as analyses that separate the mean field and wave field using low-pass filters and third-order polynomial fit (e.g., Tsuda et al. 1994; Sato et al. 2003). In this section, we focus on inertia gravity waves which have small vertical wavelengths and are known to be a driving force of the atmospheric general circulation. However, the horizontal scale of the gravity waves is too broad to understand their characters and activities in detail from single profiles, and observations, models, and theoretical studies have been actively conducted to provide a more complete description. In some studies of gravity waves, the time–height distribution of energy and frequency characteristics of gravity waves have been investigated using long-term radiosonde observation data (e.g., Fritts and Alexander 2003).

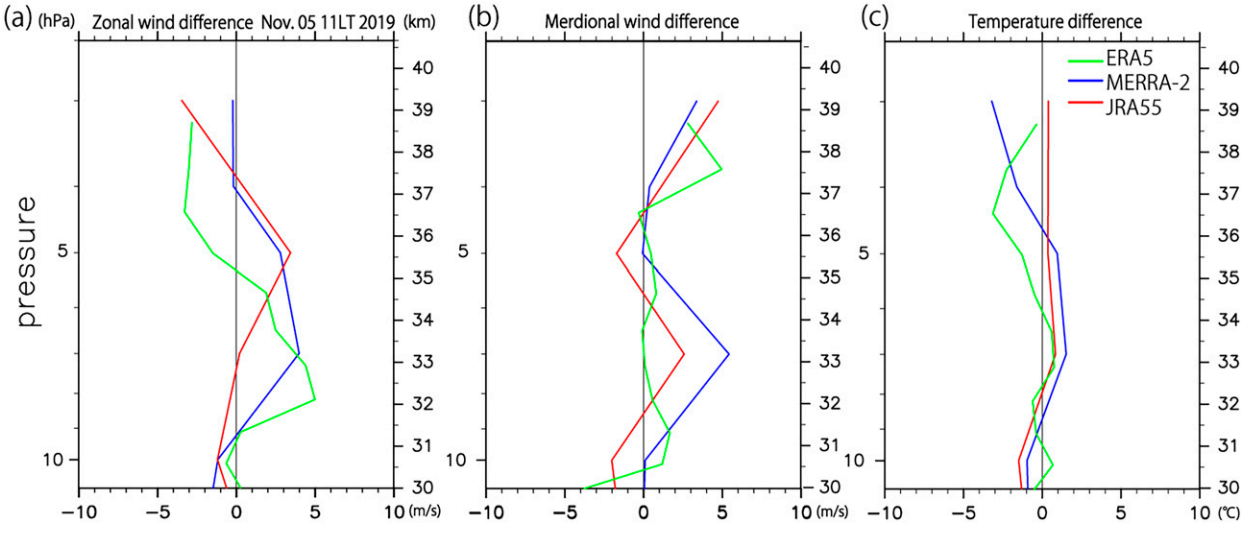

FIG. 8. Vertical profiles of the differences for (a) zonal wind, (b) meridional wind, and (c) temperature between radiosonde observation data and reanalysis data (ERA5 in green, MERRA-2 in blue, and JRA-55 in red).

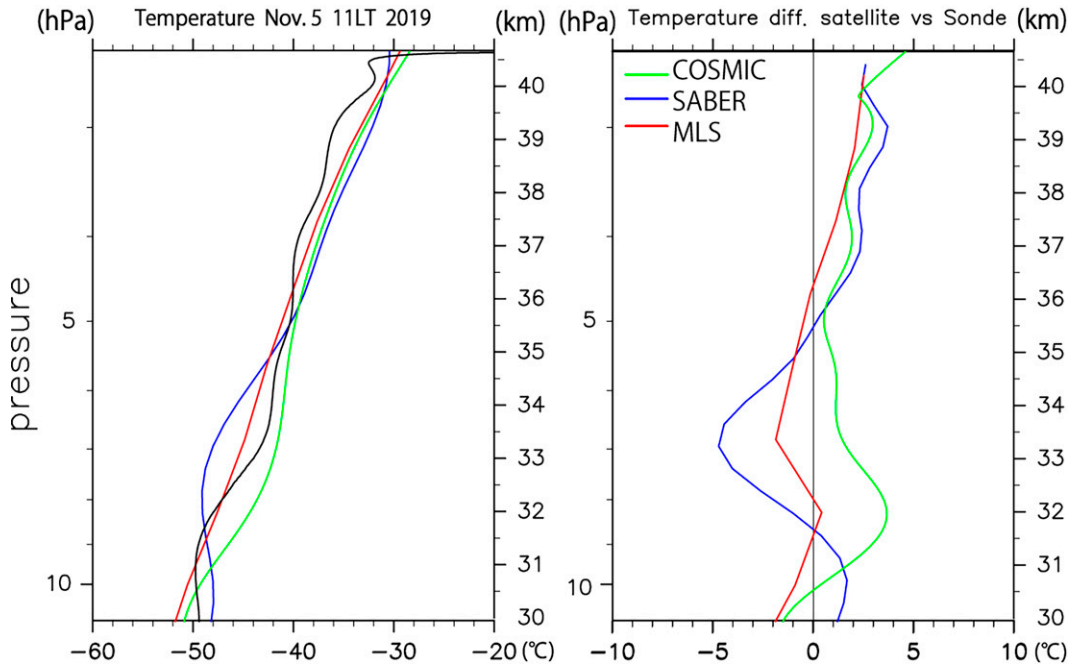

FIG. 9. Vertical profiles of (left) temperature and (right) temperature difference between satellite data and radiosonde observation data at 1100 JST 5 Nov 2019. The green line is COSMIC, the blue line is SABER, the red line is MLS, and the black line is radiosonde observation data.

Hodograph analysis, which is applied to the wavy structure seen in the middle atmosphere, is a well-established method to investigate the characteristics of gravity waves using radiosonde observations, rocketsonde observations, and large atmospheric radars (e.g., Hirota and Niki 1986; Sato 1994; Tateno and Sato 2008). For this analysis, data with a vertical resolution finer than at least 200 m are desirable. Therefore, it is important to obtain radiosonde data with an altitude of over 40 km to study gravity wave activity. To investigate the characteristics of inertial gravity waves, it is useful to pay attention to the structure of the background field and to use hodograph analysis, the Stokes parameter analysis, and the dispersion relation (e.g., Eckermann 1996; Lane et al. 2003; Tateno and Sato 2008). We conducted the hodograph analysis and the Stokes parameter analysis to estimate the wave parameters of inertial gravity waves, such as vertical wavelength, intrinsic period, and horizontal wavelength, in this section. From Fig. 2, it is indicated that the disturbances observed in the layer 39–40 km have vertical wavelengths of order 2 km, with eddy amplitudes of ~5 m s^{-1} and ~2 K. When a bandpass filter for wavelengths of 1–4 km is applied to the radiosonde data, remarkable, regular disturbances can be seen in the layer 39–40 km (Fig. 10). The hodograph of gravity wave has a shape of an ellipse under the linear theory. The direction of major axis expresses the direction of wave propagation with a 180° ambiguity. The lengths of the major and minor axes of the ellipse correspond to the amplitudes of gravity wave wind components parallel to ($\tilde{u}$) and perpendicular to ($\tilde{v}$), respectively. From the polarization relation, the intrinsic period or frequency is obtained as follows:

$$\tilde{v} = -i\frac{f}{\hat{\omega}}\tilde{u}, \quad T_{\hat{\omega}} = \frac{2\pi}{\hat{\omega}}, \tag{1}$$

$$\tilde{u} = \hat{u}\sin(mz), \quad \tilde{v} = \hat{v}\cos(mz), \quad \lambda_m = \frac{2\pi}{m}, \tag{2}$$

where f is the Coriolis parameter, $\hat{\omega}$ is the intrinsic frequency, $T_{\hat{\omega}}$ is the intrinsic period, $\hat{u}$ and $\hat{v}$ are amplitudes of $\tilde{u}$ and $\hat{v}$, respectively, m is the vertical wavenumber, and λ_m is the vertical wavelength. The dispersion relation of gravity waves under the hydrostatic assumption is written as

$$\hat{\omega}^2 = f^2 + \frac{N^2K^2}{m^2}, \quad \lambda_K = \frac{2\pi}{K}, \tag{3}$$

where N^2 is the static stability, K is the horizontal wavenumber, and λ_K is the horizontal wavelength. Thus, the vertical wavelength and intrinsic period are obtained from (1) and (2), and the horizontal wavelength is obtained from the dispersion relation (3). The intrinsic horizontal and vertical group velocities ($\hat{C}_{gh}$, $\hat{C}_{gz}$) can be also obtained by using the dispersion relation (3) as follows:

$$\hat{C}_{gh} = \frac{K}{\hat{\omega}}\frac{N^2}{m^2}, \tag{4}$$

$$\hat{C}_{gz} = -\frac{m}{\hat{\omega}}\frac{\hat{\omega}^2 - f^2}{m^2}. \tag{5}$$

A more detailed hodograph analysis is shown in Tateno and Sato (2008). Note that neglect of basic state winds in this formulation may by justified in this case since basic state winds above 22 km are fairly weak.

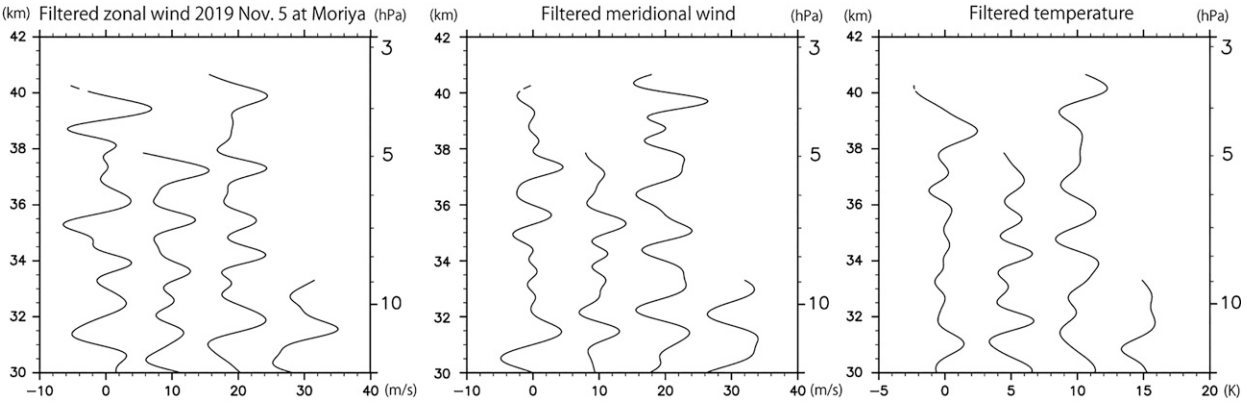

FIG. 10. Time series of vertical profiles of bandpass filtered (left) zonal wind, (center) meridional wind, and (right) temperature. Each subsequent profile is displaced by +10 m s^{-1} for zonal and meridional winds and by +5°C for temperature.

Figure 11 shows hodographs at the height of 39–40 km at 1700 and 2300 JST 5 November. The abscissa and ordinate show the zonal and meridional wind velocities, respectively. The ellipses were calculated by applying the least squares method to the bandpass filtered wind velocity data. Both hodographs show clockwise rotation with height, which suggests upward energy propagation in the Northern Hemisphere. The estimated vertical wavelengths are about 1.7 and 1.3 km, and intrinsic periods are about 6.1 and 7.4 h. The estimated horizontal wavelengths are about 129 and 123 km. Note that the mean zonal wind and the static stability used to determine the horizontal wavelength is calculated using the data that are averaged over two temperature observations with a low-pass filter of 4 km in the vertical direction and are averaged for 38.5–40.5 km. The estimated intrinsic horizontal group velocities are about 5.3 and 4.0 m s^{-1}. The estimated vertical velocities are about 7.0×10^{-2} and 4.2×10^{-2} m s^{-1}. Mean square errors due to the ellipse fitting on respective wave parameters are 0.08 and 0.19. The estimated wave parameters are summarized in Table 2. Note that both extracted waves have large amplitudes of 5.79 and 6.01 m s^{-1}, which are adequate for meaningful analysis.

The vertical wind velocities of gravity waves are estimated by substituting obtained horizontal and vertical wavenumbers, and horizonal wave amplitude into the continuity equation, which is about 76 and 64 mm s^{-1}, respectively, for these two profiles. On the other hand, vertical wind velocities may be estimated by using the thermodynamic equation for perturbations, which is written as

$$\hat{\theta} = \frac{\overline{\theta}_z}{\hat{\omega}} \hat{w} , \tag{6}$$

where $\hat{\theta}$ and $\hat{w}$ are the amplitude of potential temperature and vertical wind velocity of perturbations, $\overline{\theta}_z$ is the vertical derivative of the mean potential temperature. From the Fig. 10 and pressure, the amplitudes of potential temperature

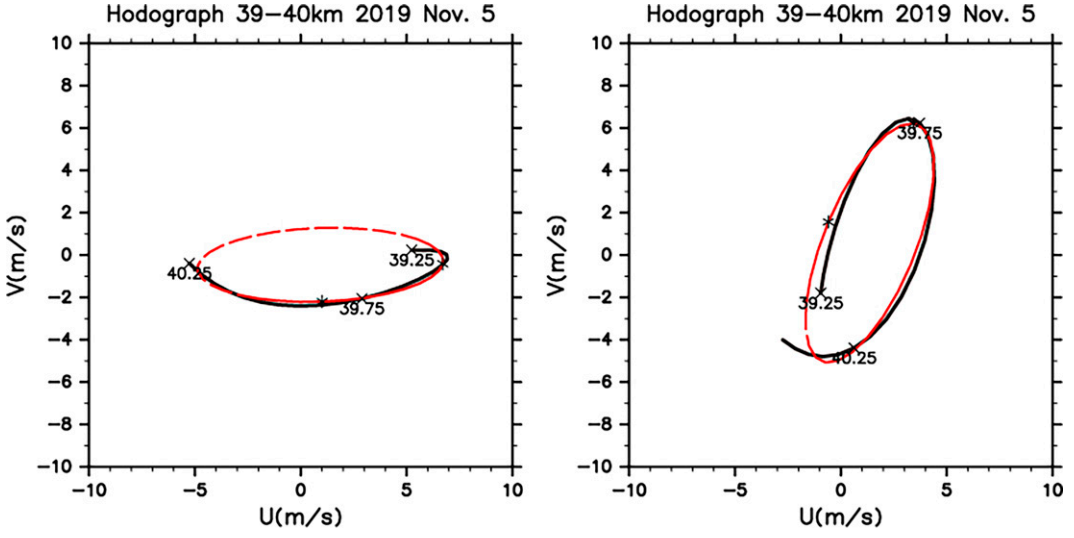

FIG. 11. Hodographs of the bandpass filtered horizontal wind velocity in the 39–40-km layer at (left) 1700 and (right) 2300 JST 5 Nov, with fitted ellipses (red). Numbers near cross marks indicate heights at 500-m intervals.

TABLE 2. Wave parameters for two gravity waves estimated using a hodograph analysis on 5 Nov 2019.

	1700 LT	2300 LT
Vertical wavelength (km)	1.7	1.3
Intrinsic period (h)	6.1	7.4
Horizontal wavelength (km)	129	123
Horizontal and vertical group velocities (m s^{-1})	5.3 and 7.0 $\times$ 10^{-2}	4.0 and 4.2 $\times$ 10^{-2}
Horizontal and vertical energy propagation	Eastward and upward	Southwestward or south-southwestward and upward

disturbances from 38 to 40 km are about 12 and 11 K, respectively. Here, we use $(p_s/p)^{\kappa} \sim 5$, where p and p_s are the pressure and surface pressure, and $\kappa = 2/7$. When the term $\overline{\theta}_z$ is calculated in the same averaging as the static stability, the estimated gravity wave eddy vertical velocities are 54 and 50 mm s^{-1}, which is roughly consistent with that estimated from horizonal wind velocity in the continuity equation. In addition, the aspect ratio of vertical and horizontal wavelengths of both waves is larger than 100, which is consistent with the assumption of the hydrostatic balance used in the dispersion relation for gravity waves.

Next, we estimated another wave parameters from the Stokes parameter analysis. The four Stokes parameters can be defined as (Eckermann 1996; Murphy et al. 2014)

$$I = \overline{u'^2} + \overline{v'^2}, \tag{7}$$

$$D = \overline{u'^2} - \overline{v'^2}, \tag{8}$$

$$P = 2\overline{u'v'}, \tag{9}$$

$$Q = 2\overline{u'v'_H}, \tag{10}$$

where u' and v' are perturbation zonal and meridional wind velocities, v'_H is the Hilbert transform of perturbation meridional wind velocity, I is the total variance, D is the axial anisotropy, P is "in phase" covariance, and Q is "in quadrature" covariance. Moreover, the horizontal propagation direction of the gravity wave Θ is obtained as follows:

$$\Theta = \frac{1}{2}\arctan\left(\frac{P}{D}\right). \tag{11}$$

In this study, the Stokes parameters are calculated by applying a 4-km low-pass filter in the vertical to the bandpass filtered radiosonde data. Figure 12 shows the vertical profiles of Stokes parameters at 1700 and 2300 JST 5 November. It is found that D is close to I, P is almost zero, and Q is positive from 38 to 40 km at 1700 JST since the perturbation meridional wind velocity is small. Note that the positive Q express upward propagation of gravity waves in the Northern Hemisphere. On the other hand, D is negative, P is positive and large, and Q is positive at 2300 JST. These results show a good correspondence with the characteristics obtained from the hodograph analysis.

Focusing on the horizontal propagation Θ from 38 to 40 km, it is found that the direction is eastward at 1700 JST and southwestward or south-southwestward at 2300 JST. From the estimated propagation direction and group velocity, the source of gravity waves is briefly discussed. In the troposphere during the observation period, a cold front was passing from west to east to the north of the Tsukuba release field,

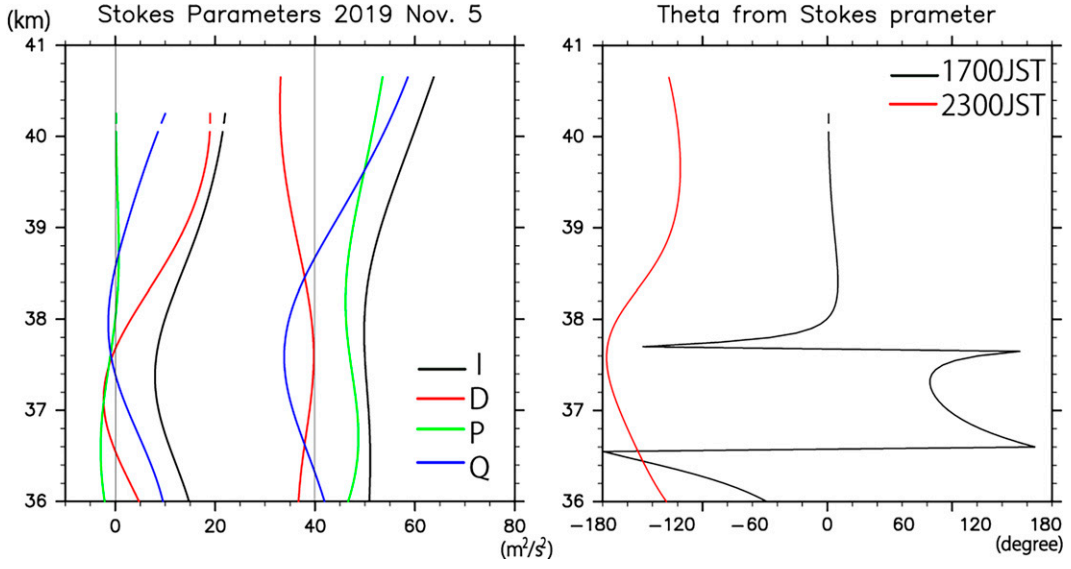

FIG. 12. Vertical profiles of (left) Stokes parameters I (black), D (red), P (green), and Q (blue) and (right) horizontal propagation direction of gravity waves at 1700 JST (black) and 2300 JST (red) 5 Nov.

as the low pressure system propagated eastward around Hokkaido. This is one of the possible candidates for the excitation source of gravity waves. In the stratosphere, the polar night jet was located to the north of northwest of Japan, and the strong wind field was gradually moving to the east. The strong polar night jet is the second possible candidate for the excitation source of gravity waves. Note that further analysis, such as ray tracing, is needed to identify the excitation source of gravity waves in more detail.

4. Conclusions

In this study, high-resolution wind velocity and temperature data above a height of 40 km are obtained by experimental radiosonde observations at the Tsukuba release field, Japan. From the four experimental observations, it is indicated that the condition for observing at the height of more than 40 km is to set the buoyancy to a value of 1600–2000 g using the TX3000 (3000-g balloon). Comparison of the obtained radiosonde data with satellite data and reanalysis data showed that useful wind velocity and temperature data may be readily obtained in the 30–40-km layer. Observation of the upper stratosphere by radiosondes is important for understanding the wave activity which drives the general circulation of the middle atmosphere. Specifically, momentum fluxes, wave energy and wave activity density can be estimated from the wind and temperature components of the waves in the observed altitude region. Also, high-altitude radiosonde observations are important to better understand the variation in representing the SAO among different reanalysis datasets. In the future, we plan to carry out high-altitude radiosonde observations for a long time or at multiple points (e.g., the YMC campaign) based on the results of this experimental observation. We expect that combining satellite and high-altitude observations will make it possible to capture the wave activity in the middle atmosphere in more detail.

Acknowledgments. The authors would like to acknowledge use of wind and temperature profiles from the following global datasets: ERA5 data, available from https://cds.climate.copernicus.eu/cdsapp#!/dataset/reanalysis-era5-pressure-levels?tab=overview, MERRA-2 assimilated meteorological fields V5.12.4, available from https://goldsmr5.gesdisc.eosdis.nasa.gov/data/MERRA2/M2I3NPASM.5.12.4/2019/11/, JRA-55 data from https://jra.kishou.go.jp/JRA-55/index_en.html#usage, as well as COSMIC temperature data, available from https://data.cosmic.ucar.edu/gnss-ro/cosmic2/nrt/level2/2019/310/atmPrf_nrt_2019_310.tar.gz, SABER temperature data, from ftp://saber.gatsinc.com/custom/Temp_O3_H2O/v2.0/SABER_Temp_O3_H2O_November2019_v2.0.nc, and MLS temperature data from https://acdisc.gesdisc.eosdis.nasa.gov/data/Aura_MLS_Level2/ML2T.004/2019/MLS-Aura_L2GP-Temperature_v04-23-c01_2019d310.he5. The high-altitude radiosonde observation data are available from the YMC data repository at http://www.jamstec.go.jp/ymc/. We thank Dr. Kirsti Salonen and anonymous reviewers for providing constructive comments and suggestions. The GFD-DENNOU library was used for drawing figures. Part of this study was supported by a Grant-in-Aid for Young Scientists 18K13616 of the Japan Society for the Promotion of Science (JSPS). MHH acknowledges support from National Science Foundation Grant AGS 1947658.

REFERENCES

Baldwin, M. P., and L. J. Gray, 2005: Tropical stratospheric zonal winds in ECMWF ERA-40 reanalysis, rocketsonde data and rawinsonde data. *Geophys. Res. Lett.*, **32**, L09806, https://doi.org/10.1029/2004GL022328.

——, and Coauthors, 2001: The quasi-biennial oscillation. *Rev. Geophys.*, **39**, 179–229, https://doi.org/10.1029/1999RG000073

——, and Coauthors, 2021: Sudden stratospheric warmings. *Rev. Geophys.*, **59**, e2020RG000708, https://doi.org/10.1029/2020RG000708.

Baron, P., D. Murtagh, P. Eriksson, J. Mendrok, S. Ochiai, K. Pérot, H. Sagawa, and M. Suzuki, 2018: Simulation study for the Stratospheric Inferred Winds (SIW) sub-millimeter limb sounder. *Atmos. Meas. Tech.*, **11**, 4545–4566, https://doi.org/10.5194/amt-11-4545-2018.

Butchart, N., 2014: The Brewer-Dobson circulation. *Rev. Geophys.*, **52**, 157–184, https://doi.org/10.1002/2013RG000448.

Das, S. S., K. N. Uma, V. N. Bineesha, K. V. Suneeth, and G. Ramkumar, 2016: Four-decadal climatology intercomparison of rocketsonde and radiosonde with different reanalysis data: Results from Thumba equatorial station. *Quart. J. Roy. Meteor. Soc.*, **142**, 91–101, https://doi.org/10.1002/qj.2632.

Dörnbrack, A., and Coauthors, 2018: Gravity waves excited during a minor sudden stratospheric warming. *Atmos. Chem. Phys.*, **18**, 12 915–12 931, https://doi.org/10.5194/acp-18-12915-2018.

Eckermann, S. D., 1996: Hodographic analysis of gravity waves: Relationships among Stokes parameters, rotary spectra and cross-spectral methods. *J. Geophys. Res.*, **101**, 19 169–19 174, https://doi.org/10.1029/96JD01578.

Fritts, D. C., and M. J. Alexander, 2003: Gravity wave dynamics and effects in the middle atmosphere. *Rev. Geophys.*, **41**, 1003, https://doi.org/10.1029/2001RG000106.

Froidevaux, L., and Coauthors, 2006: Early validation analyses of atmospheric profiles from EOS MLS on the Aura satellite. *IEEE Trans. Geosci. Remote Sens.*, **44**, 1106–1121, https://doi.org/10.1109/TGRS.2006.864366.

Fukao, S., T. Sato, T. Tsuda, S. Kato, K. Wakasugi, and T. Makihira, 1985: The MU radar with an active phased array system, 1. Antenna and power amplifiers. *Radio Sci.*, **20**, 1155–1168, https://doi.org/10.1029/RS020i006p01155.

Fuke, H., 2017: Recent highlights of scientific ballooning in Japan. *J. Astron. Instrum.*, **6**, 1740001, https://doi.org/10.1142/S2251171717400013.

Gallice, A., F. G. Wienhold, C. R. Hoyle, F. Immler, and T. Peter, 2011: Modeling the ascent of sounding balloons: Derivation of the vertical air motion. *Atmos. Meas. Tech.*, **4**, 2235–2253, https://doi.org/10.5194/amt-4-2235-2011.

GMAO, 2015: MERRA-2 inst3_3d_asm_Np: 3D, 3-hourly, instantaneous, pressure-level, assimilation, assimilated meteorological fields, V5.12.4. GES DISC, accessed 5 December 2020, https://doi.org/10.5067/QBZ6MG944HW0.

Hersbach, H., and Coauthors, 2018: Operational global reanalysis: Progress, future directions and synergies with NWP. ECMWF ERA Rep. 27, 65 pp., https://www.ecmwf.int/node/18765.

Hirota, I., 1980: Observational evidence of the semiannual oscillation in the tropical middle atmosphere—A review. *Pure Appl. Geophys.*, **118**, 217–238, https://doi.org/10.1007/BF01586452.

——, and T. Niki, 1986: Inertia-gravity waves in the troposphere and stratosphere observed by the MU radar. *J. Meteor. Soc. Japan*, **64**, 995–999, https://doi.org/10.2151/jmsj1965.64.6_995.

Hitchman, M. H., and C. B. Leovy, 1986: Evolution of the zonal mean state in the equatorial middle atmosphere during October 1978–May 1979. *J. Atmos. Sci.*, **43**, 3159–3176, https://doi.org/10.1175/1520-0469(1986)043<3159:EOTZMS>2.0.CO;2.

Kawatani, Y., T. Hirooka, K. Hamilton, A. K. Smith, and M. Fujiwara, 2020: Representation of the equatorial stratopause semiannual oscillation in global atmospheric reanalyses. *Atmos. Chem. Phys.*, **20**, 9115–9133, https://doi.org/10.5194/acp-20-9115-2020.

Kizu, N., T. Sugidachi, E. Kobayashi, S. Hoshino, K. Shimizu, R. Maeda, and M. Fujiwara, 2018: Technical characteristics and GRUAN data processing for the Meisei RS-11G and iMS-100 radiosondes. GRUAN Tech. Doc. GRUAN-TD-5, v1.0, 153 pp., http://hdl.handle.net/2115/72249.

Kobayashi, S., and Coauthors, 2015: The JRA-55 Reanalysis: General specifications and basic characteristics. *J. Meteor. Soc. Japan*, **93**, 5–48, https://doi.org/10.2151/jmsj.2015-001.

Kodera, K., N. Eguchi, J. N. Lee, Y. Kuroda, and S. Yukimoto, 2011: Sudden changes in the tropical stratospheric and tropospheric circulation during January 2009. *J. Meteor. Soc. Japan*, **89**, 283–290, https://doi.org/10.2151/jmsj.2011-308.

Lane, T. P., M. J. Reeder, and F. M. Guest, 2003: Convectively generated gravity waves observed from radiosonde data taken during MCTEX. *Quart. J. Roy. Meteor. Soc.*, **129**, 1731–1740, https://doi.org/10.1256/qj.02.196.

Mlynczak, M. G., B. T. Marshall, F. J. Martin-Torres, J. M. Russell, R. E. Thompson, E. E. Remsberg, and L. L. Gordley, 2007: Sounding of the atmosphere using broadband emission radiometry observations of daytime mesospheric $O_2(^1\Delta)$ 1.27 μm emission and derivation of ozone, atomic oxygen, and solar and chemical energy deposition rates. *J. Geophys. Res.*, **112**, D15306, https://doi.org/10.1029/2006JD008355.

Murphy, D. J., S. P. Alexander, A. R. Klekociuk, P. T. Love, and R. A. Vincent, 2014: Radiosonde observations of gravity waves in the lower stratosphere over Davis, Antarctica. *J. Geophys. Res. Atmos.*, **119**, 11 973–11 996, https://doi.org/10.1002/2014JD022448.

Murtagh, D., and Coauthors, 2002: An overview of the Odin atmospheric mission. *Can. J. Phys.*, **80**, 309–319, https://doi.org/10.1139/p01-157.

Nishimoto, E., and S. Yoden, 2017: Influence of the stratospheric quasi-biennial oscillation on the Madden–Julian oscillation during austral summer. *J. Atmos. Sci.*, **74**, 1105–1125, https://doi.org/10.1175/JAS-D-16-0205.1.

Park, B. C., and Coauthors, 2006: Algorithm improvement and validation of National Institute for Environmental Studies ozone differential absorption lidar at the Tsukuba Network for Detection of Stratospheric Change complementary station. *Appl. Opt.*, **45**, 3561–3576, https://doi.org/10.1364/AO.45.003561.

Reber, C. A., C. E. Trevathan, R. J. McNeal, and M. R. Luther, 1993: The Upper Atmosphere Research Satellite (UARS) mission. *J. Geophys. Res.*, **98**, 10 643–10 647, https://doi.org/10.1029/92JD02828.

Russell, J. M., III, M. G. Mlynczak, L. L. Gordley, J. Tansock, and R. Esplin, 1999: An overview of the SABER experiment and preliminary calibration results. *Proc. SPIE*, **3756**, 277–288, https://doi.org/10.1117/12.366382.

Sato, K., 1994: A statistical study of the structure, saturation and sources of inertio-gravity waves in the lower stratosphere observed with the MU radar. *J. Atmos. Terr. Phys.*, **56**, 755–774, https://doi.org/10.1016/0021-9169(94)90131-7.

——, D. J. O'Sullivan, and T. J. Dunkerton, 1997: Low-frequency inertia-gravity waves in the stratosphere revealed by three-week continuous observation with the MU radar. *Geophys. Res. Lett.*, **24**, 1739–1742, https://doi.org/10.1029/97GL01759.

——, M. Yamamori, S. Ogino, N. Takahashi, Y. Tomikawa, and T. Yamaouchi, 2003: A meridional scan of the stratospheric gravity wave field over the ocean in 2001 (MeSSO2001). *J. Geophys. Res.*, **108**, 4491, https://doi.org/10.1029/2002JD003219.

——, and Coauthors, 2014: Program of the Antarctic Syowa MST/IS radar (PANSY). *J. Atmos. Sol.-Terr. Phys.*, **118**, 2–15, https://doi.org/10.1016/j.jastp.2013.08.022.

Schwartz, M., N. Livesey, and W. Read, 2015: MLS/Aura level 2 temperature, V004. GES DISC, accessed 27 April 2020, https://doi.org/10.5067/Aura/MLS/DATA2021.

Stroud, W. G., 1960: Initial results of the TIROS I meteorological satellite. *J. Geophys. Res.*, **65**, 1643–1643, https://doi.org/10.1029/JZ065i005p01643.

Tateno, S., and K. Sato, 2008: A study of inertia-gravity waves in the middle stratosphere based on intensive radiosonde observations. *J. Meteor. Soc. Japan*, **86**, 719–732, https://doi.org/10.2151/jmsj.86.719.

Tiefenau, H. K. E., and A. Gebbeken, 1989: Influence of meteorological balloons on temperature measurements with radiosondes: Nighttime cooling and daylight heating. *J. Atmos. Oceanic Technol.*, **6**, 36–42, https://doi.org/10.1175/1520-0426(1989)006<0036:IOMBOT>2.0.CO;2.

Tsuda, T., Y. Murayama, H. Wiryosumarto, S. W. B. Harijono, and S. Kato, 1994: Radiosonde observations of equatorial atmosphere dynamics over Indonesia, 1. Equatorial waves and diurnal tides. *J. Geophys. Res.*, **99**, 10 491–10 505, https://doi.org/10.1029/94JD00355.

UCAR COSMIC Program, 2019: COSMIC-2 data products 11/09/2019. UCAR/NCAR COSMIC, accessed 5 December 2020, https://doi.org/10.5065/T353-C093.

WMO, 1957: Definition of the tropopause. *WMO Bull.*, **6**, 136.

Yoneyama, K., and C. Zhang, 2020: Years of the Maritime Continent. *Geophys. Res. Lett.*, **47**, e2020GL087182, https://doi.org/10.1029/2020GL087182.

Zhou, L., Z. Sheng, Z. Fan, and Q. Liao, 2017: Data analysis of the TK-1G sounding rocket installed with a satellite navigation system. *Atmosphere*, **8**, 199, https://doi.org/10.3390/atmos8100199.

Zink, F., and R. A. Vincent, 2001: Wavelet analysis of stratospheric gravity wave packets over Macquarie Island: 2. Intermittency and mean-flow accelerations. *J. Geophys. Res.*, **106**, 10 289–10 297, https://doi.org/10.1029/2000JD900846.